# Rossby Wave Instability and Apparent Phase Speeds in Large Ocean Basins

P. E. ISACHSEN

*Department of Geosciences, University of Oslo, Oslo, Norway*

J. H. LaCASCE

*Department of Geosciences, University of Oslo, and Norwegian Meteorological Institute, Oslo, Norway, and Woods Hole Oceanographic Institution, Woods Hole, Massachusetts*

J. PEDLOSKY

*Woods Hole Oceanographic Institution, Woods Hole, Massachusetts*

ABSTRACT

The stability of baroclinic Rossby waves in large ocean basins is examined, and the quasigeostrophic (QG) results of LaCasce and Pedlosky are generalized. First, stability equations are derived for perturbations on large-scale waves, using the two-layer shallow-water system. These equations resemble the QG stability equations, except that they retain the variation of the internal deformation radius with latitude. The equations are solved numerically for different initial conditions through eigenmode calculations and time stepping. The fastest-growing eigenmodes are intensified at high latitudes, and the slower-growing modes are intensified at lower latitudes. All of the modes have meridional scales and growth times that are comparable to the deformation radius in the latitude range where the eigenmode is intensified. This is what one would expect if one had applied QG theory in latitude bands. The evolution of large-scale waves was then simulated using the Regional Ocean Modeling System primitive equation model. The results are consistent with the theoretical predictions, with deformation-scale perturbations growing at rates inversely proportional to the local deformation radius. The waves succumb to the perturbations at the mid- to high latitudes, but are able to cross the basin at low latitudes before doing so. Also, the barotropic waves produced by the instability propagate faster than the baroclinic long-wave speed, which may explain the discrepancy in speeds noted by Chelton and Schlax.

## 1. Introduction

Quasigeostrophic (QG) studies suggest that baroclinic Rossby waves are unstable (Jones 1979; Vanneste 1995; LaCasce and Pedlosky 2004, hereinafter LP04). The waves break into deformation-scale eddies on a time scale that is proportional to the ratio of the deformation radius to the shear velocity, that is, $T_g \propto L_D/U$. Instability occurs because waves that are generated at the eastern oceanic boundary tend to have a north–south orientation, and thus cannot be stabilized by the

*Corresponding author address:* Joe LaCasce, Norwegian Meteorological Institute, P.O. Box 43, Blindern, Oslo 0313, Norway.
E-mail: jlacasce@met.no

$\beta$ effect (Pedlosky 1987). Because the instability occurs for essentially *all* oceanic Rossby waves regardless of amplitude or latitude, the only question is how long it will be before the wave succumbs to instability. In other words, if a Rossby wave emanates from the eastern boundary of the basin can it cross to the western boundary before disintegrating?

The answer depends on the ratio of the crossing time to the unstable growth time, defined as $Z$ by LP04. Because the crossing for a long baroclinic wave is $L_B(\beta L_D^2)^{-1}$ (where $L_B$ is the basin width), we have

$$Z \equiv \frac{T_R}{T_g} = \frac{U L_B}{\beta L_D^3}. \tag{1}$$

Waves can cross intact if $Z$ is less than order 1.

The theory of LP04 makes three specific predictions vis-à-vis the oceanic Rossby wave field. First, large-scale baroclinic waves should be seen only at low latitudes, where $Z$ is small. Because $Z$ varies as the inverse deformation radius cubed, the latitudinal transition between the crossing and disintegrating waves is sharp. Using representative values for the Pacific Ocean, LP04 suggested this critical latitude is about 20°. This is roughly consistent with satellite observations of sea surface height, where large-scale propagation is only visible at latitudes lower than about 20° (Chelton and Schlax 1996).

Second, the dominant eddy scale north of the critical latitude (in the Northern Hemisphere) should be larger than the deformation radius. This is because the most unstable mode has a meridional scale of roughly 2 times the deformation radius. Such a shift in scale is also in accord with satellite observations (Stammer 1997). If, in addition, the barotropic eddies produced by instability merge, they will produce still-larger barotropic waves. This can be seen in numerical experiments when $Z > 1$ (LP04).

Third, the westward phase propagation observed at the mid- and high latitudes should occur at speeds faster than the baroclinic long-wave speed. This is because the most unstable barotropic waves propagate faster than long baroclinic waves. This, too, is in agreement with satellite observations (Chelton and Schlax 1996). If eddy merger occurs, yielding larger barotropic waves, still-higher speeds will occur.

Thus, in these respects, the theory agrees with observations. However, it is not strictly correct to apply QG theory to large basins. The QG theory assumes the deformation radius is constant and this is certainly not the case; in the Pacific, the deformation radius varies from several hundred kilometers at low latitudes to a few kilometers at high latitudes. LP04 suggested that the QG results should apply *locally*, over a latitude band, and could thus be used to infer the behavior of large-scale waves in a piecewise fashion. But, this remains to be demonstrated.

Hereinafter we consider the stability of baroclinic Rossby waves in large basins, like the Pacific. We first extend the QG theory to larger basins by allowing for basic baroclinic waves that obey the shallow-water equations. This yields a set of equations that can be integrated numerically to determine the wave stability. We then use the Regional Ocean Modeling System (ROMS) primitive equation model to study the evolution of similar large baroclinic waves. The results of these computations are consistent with the theory.

## 2. The LQG model

### a. Equations

We assume a two-layer ocean under the shallow-water approximation (e.g., Pedlosky 1987):

$$\frac{\partial}{\partial t}\mathbf{u}_1 + \mathbf{u}_1 \cdot \nabla\mathbf{u}_1 + f\mathbf{k} \times \mathbf{u}_1 = -g\nabla\chi \quad \text{and} \tag{2}$$

$$\frac{\partial}{\partial t}\mathbf{u}_2 + \mathbf{u}_2 \cdot \nabla\mathbf{u}_2 + f\mathbf{k} \times \mathbf{u}_2 = -g\nabla\chi - g'\nabla\eta, \tag{3}$$

where $\mathbf{u}_1$ and $\mathbf{u}_2$ are the layer velocities, $\chi$ is the sea surface height, and $\eta$ is the interface height. From these layer equations, we derive the following equations for the barotropic ($B$) and baroclinic ($T$) velocities:

$$\frac{\partial}{\partial t}\mathbf{u}_B + \mathbf{u}_B \cdot \nabla\mathbf{u}_B + \frac{1}{4}\mathbf{u}_T \cdot \nabla\mathbf{u}_T + f\mathbf{k} \times \mathbf{u}_B =$$

$$-g\nabla\chi - \frac{1}{2}g'\nabla\eta \equiv -\nabla\phi_B \quad \text{and} \tag{4}$$

$$\frac{\partial}{\partial t}\mathbf{u}_T + \mathbf{u}_T \cdot \nabla\mathbf{u}_B + \mathbf{u}_B \cdot \nabla\mathbf{u}_T + f\mathbf{k} \times \mathbf{u}_T =$$

$$-g'\nabla\eta \equiv -\nabla\varphi_T, \tag{5}$$

where

$$\mathbf{u}_B \equiv \frac{1}{2}(\mathbf{u}_1 + \mathbf{u}_2) \quad \text{and} \quad \mathbf{u}_T \equiv (\mathbf{u}_2 - \mathbf{u}_1) \tag{6}$$

are the barotropic and baroclinic velocities, respectively. We have taken the layers to have equal depths of $H/2$ (a simplifying assumption that does not alter the results qualitatively). Notice that we have defined the following equivalent barotropic and baroclinic displacements:

$$\phi_B = g\chi + \frac{1}{2}g'\eta \quad \text{and} \quad \phi_T = g'\eta, \tag{7}$$

to separate the pressure gradient terms on the RHS of the equations.

The layer-continuity equations are

$$\frac{\partial}{\partial t}(H/2 + \chi - \eta) + \nabla \cdot [\mathbf{u}_1(H/2 + \chi - \eta)] = 0 \tag{8}$$

and

$$\frac{\partial}{\partial t}(H/2 + \eta) + \nabla \cdot [\mathbf{u}_2(H/2 + \eta)] = 0. \tag{9}$$

We can rewrite these in terms of the barotropic and baroclinic velocities and displacements as follows:

$$\frac{\partial}{\partial t}\phi_T + \frac{g'H}{2}\boldsymbol{\nabla}\cdot\left(\mathbf{u}_B + \frac{1}{2}\mathbf{u}_T\right) + \boldsymbol{\nabla}\cdot\left[\left(\mathbf{u}_B + \frac{1}{2}\mathbf{u}_T\right)\phi_T\right] = 0 \qquad (10)$$

and

$$\frac{g'}{g}\frac{\partial}{\partial t}\phi_B + \left(\frac{g'}{4g} + 1\right)g'H\boldsymbol{\nabla}\cdot\mathbf{u}_B + \frac{g'}{8g}g'H\boldsymbol{\nabla}\cdot\mathbf{u}_T + \left(\frac{g'}{4g} + 1\right)\boldsymbol{\nabla}\cdot(\mathbf{u}_T\phi_T) + \frac{g'}{g}\boldsymbol{\nabla}\cdot\left[\left(\mathbf{u}_B - \frac{1}{2}\mathbf{u}_T\right)\phi_B\right] = 0. \qquad (11)$$

We will nondimensionalize the equations to facilitate the subsequent perturbation expansions. We assume a velocity scale $U$, a length scale $L$, and an advective time scale $T = L/U$. The resulting equations are then

$$\epsilon\frac{\partial}{\partial t}\mathbf{u}_B + \epsilon\mathbf{u}_B\cdot\nabla\mathbf{u}_B + \frac{\epsilon}{4}\mathbf{u}_T\cdot\nabla\mathbf{u}_T + f\mathbf{k}\times\mathbf{u}_B = -\nabla\phi_B, \qquad (12)$$

$$\epsilon\frac{\partial}{\partial t}\mathbf{u}_T + \epsilon\mathbf{u}_T\cdot\nabla\mathbf{u}_B + \epsilon\mathbf{u}_B\cdot\nabla\mathbf{u}_T + f\mathbf{k}\times\mathbf{u}_T = -\nabla\phi_T, \qquad (13)$$

$$\epsilon F_T\frac{\partial}{\partial t}\phi_T + \frac{1}{2}\boldsymbol{\nabla}\cdot\left(\mathbf{u}_B + \frac{1}{2}\mathbf{u}_T\right) + \epsilon F_T\boldsymbol{\nabla}\cdot\left[\left(\mathbf{u}_B + \frac{1}{2}\mathbf{u}_T\right)\phi_T\right] = 0, \quad\text{and} \qquad (14)$$

$$\epsilon F_B\frac{\partial}{\partial t}\phi_B + \boldsymbol{\nabla}\cdot\mathbf{u}_B + \frac{g'}{8g}\boldsymbol{\nabla}\cdot\mathbf{u}_T + \epsilon F_T\boldsymbol{\nabla}\cdot(\mathbf{u}_T\phi_T) + \epsilon F_B\boldsymbol{\nabla}\cdot\left[\left(\mathbf{u}_B - \frac{1}{2}\mathbf{u}_T\right)\phi_B\right] = 0, \qquad (15)$$

where the variables now are understood to be nondimensional. We have assumed that $|g\chi| \approx |g'\eta|$ and $|\phi_B| \approx |\phi_T| \approx f_0UL$. We also exploited the fact that $1 + g'/g \approx 1$. We will confine our attention to the $\beta$ plane, so that the nondimensional Coriolis parameter is $f = 1 + \beta Ly/f_0$, with $f_0$ being the parameter value at the midbasin. However, we do not assume that the $\beta$ term is small (as is usually done in QG); the basin may be large.

The solutions will depend on three nondimensional parameters:

$$\epsilon = \frac{U}{f_0L}, \quad F_B \equiv \frac{f_0^2L^2}{gH}, \quad\text{and}\quad F_T \equiv \frac{f_0^2L^2}{g'H}.$$

These are the Rossby number and the Burger numbers related to the external and internal deformation radii.

### b. Basic wave

We consider first the large-scale baroclinic wave, which we designate with capital variables ($U_T$, $V_T$, $\Phi_T$, $\Phi_B$). Because the relevant length scale is that of the basin, the Rossby number is small (for typical velocities). In addition, the barotropic Burger number $F_B$ is order 1 and the baroclinic Burger number is large; we will assume, for simplicity, that $F_T \approx \epsilon^{-1}$.

Because the wave is predominantly baroclinic, an appropriate expansion is

$$\mathbf{u}_T = \epsilon\mathbf{U}_T + \epsilon^2\mathbf{U}_T^{(2)} + \cdots, \quad \phi_T = \epsilon\Phi_T + \epsilon^2\Phi_T^{(2)} + \cdots, \qquad (16)$$

$$\mathbf{u}_B = \epsilon^2\mathbf{U}_B^{(2)} + \cdots, \quad\text{and}\quad \phi_B = \epsilon^2\Phi_B^{(2)} + \cdots. \qquad (17)$$

The leading-order wave term is order–Rossby number because if it were order 1, the wave would satisfy a Burger's equation and would thus steepen in time (e.g., Charney and Flierl 1981). One cannot assume that the barotropic part of the field is zero because self-advection by the barotropic wave excites barotropic motion at order $\epsilon^2$. Substituting these expansions into the six nondimensional equations yields, at order $|\epsilon|$,

$$f\mathbf{k}\times\mathbf{U}_T = -\nabla\Phi_T \quad\text{and} \qquad (18)$$

$$\frac{\partial}{\partial t}\Phi_T + \frac{1}{4}\boldsymbol{\nabla}\cdot\mathbf{U}_T = 0, \qquad (19)$$

which are familiar as the linearized planetary geostrophic equations. The wave velocities are geostrophic, but they are also divergent because of the variation in $f$. Combining Eqs. (18) and (19) yields the long-wave equation, which in dimensional form is

$$\frac{\partial}{\partial t}\Phi_T - \frac{g'H\beta}{4f^2}\frac{\partial}{\partial x}\Phi_T = 0. \qquad (20)$$

The solution is a steadily propagating wave with a phase speed that varies with latitude. With boundaries we require dissipation to satisfy the no-normal-flow condition, but this is a straightforward modification (e.g., LaCasce and Pedlosky 2002).

### c. Perturbations

Following LP04, we anticipate unstable growth near the deformation radius. If so, the perturbations will have a length scale that *varies with latitude*. The baroclinic Burger number is then order 1 by definition but also varies in $y$ (i.e., $F_T = f_0^2/f^2$). The barotropic Burger number also varies with latitude but is small because the external deformation radius greatly exceeds the internal radius. The Rossby number likewise varies, but we assume it is small at all latitudes. In addition, we take $\beta L_D/f$ to be small (order–Rossby number) and neglect a term proportional to $g'/g$. Under these assumptions, the first-order momentum balances are

$$\mathbf{k} \times \mathbf{u}_T = -\nabla\phi_T \quad \text{and} \quad \mathbf{k} \times \mathbf{u}_B = -\nabla\phi_B, \quad (21)$$

so that the velocities are geostrophic and nondivergent. In other words, the perturbations are *locally quasigeostrophic* (LQG). The continuity equations at first order imply that the velocities are nondivergent, meaning the system is underdetermined. Thus, one requires the next order to solve the system, a familiar feature of the QG expansion (Pedlosky 1987). Those equations can be combined into the following statement for the conservation of barotropic and baroclinic potential vorticity (PV):

$$\frac{\partial}{\partial t} q_B + \mathbf{u}_B \cdot \nabla q_B + \frac{1}{4}\mathbf{u}_T \cdot \nabla q_T + \beta\frac{\partial}{\partial x}\phi_B = 0 \quad \text{and}$$
$$(22)$$

$$\frac{\partial}{\partial t} q_T + \mathbf{u}_B \cdot \nabla q_T + \mathbf{u}_T \cdot \nabla q_B + \beta\frac{\partial}{\partial x}\phi_T = 0, \quad (23)$$

where

$$q_T \equiv \nabla^2\phi_T - 4F_T(y)\phi_T \quad \text{and} \quad q_B \equiv \nabla^2\phi_B.$$

Then, we link the perturbations to the baroclinic basic wave. To do this, we introduce into the expansion in section (2b) perturbations with a second small parameter $\alpha$,

$$\phi_T = \epsilon\Phi_T + \epsilon^2\Phi_T^{(2)} + \epsilon\alpha\phi_T + \cdots.$$

The resulting expansion yields the LQG PV equations linearized about the baroclinic basic wave:

$$\frac{\partial}{\partial t} q_B + \frac{1}{4}\mathbf{U}_T \cdot \nabla q_T + \frac{1}{4}\mathbf{u}_T \cdot \nabla Q_T + \beta\frac{\partial}{\partial x}\phi_B = 0 \quad (24)$$

and

$$\frac{\partial}{\partial t} q_T + \mathbf{U}_T \cdot \nabla q_B + \mathbf{u}_B \cdot \nabla Q_T + \beta\frac{\partial}{\partial x}\phi_T = 0, \quad (25)$$

where

$$Q_T \equiv \nabla \times \mathbf{U} - 4F_T(y)\Phi_T$$

is the basic wave potential vorticity.

Equations (24) and (25) are very similar to the QG stability equations examined by LP04. The major difference is that the baroclinic Burger number $F_T$ varies with $y$ so that the system has nonconstant coefficients.[1] This hinders simple analytical solutions, but numerical solutions are feasible and we examine some hereinafter.

## 3. LQG results

We discretized the dimensional versions of Eqs. (24) and (25) on the C grid and solved them numerically. Hereinafter we consider two types of solutions. In the first, we convert the equations to matrix form and solve the resulting eigenvalue problem. This applies to high latitudes, where the wave-crossing time is much greater than the growth time of the instabilities (the wave is stationary to first order in $1/Z$). In the second, we examine a propagating wave by stepping the equations forward in time. This applies to the full range of latitudes (and $Z$ values).

For the eigenvalue calculation, we used a wave with a vertical shear that was sinusoidal in $x$ and invariant in $y$ (except near the northern and southern boundaries, where the wave is tapered to satisfy no normal flow). In keeping with the high-$Z$ limit, we neglect the $\beta$ terms for the basic wave and the instabilities. We calculated modes for a basin 1000 km wide ($x$ direction) $\times$ 4000 km long ($y$ direction), centered at 45°N. We took the basin to be 4000 m deep, and assumed two equal depth fluid layers. We set $g' = 0.02$ m s$^{-2}$ and the wave shear at 10 cm s$^{-1}$. We extracted the first 50 eigenmodes (in complex conjugate pairs) using the sparse eigenvalue routine in Matlab.

Three eigenmodes (modes 1, 20, and 45) are shown in Fig. 1. Shown in the left panels are the barotropic eigenmodes, superimposed on the basic wave height field. At right are estimates of the corresponding meridional

---

[1] Pedlosky (1984) derived a system like this, with equations governing basin-scale motion and QG-like equations applying at the deformation scale. Theiss (2004) similarly derived a QG-like equation for a single layer with a free surface in which the latitudinal variation of the Burger number is retained.
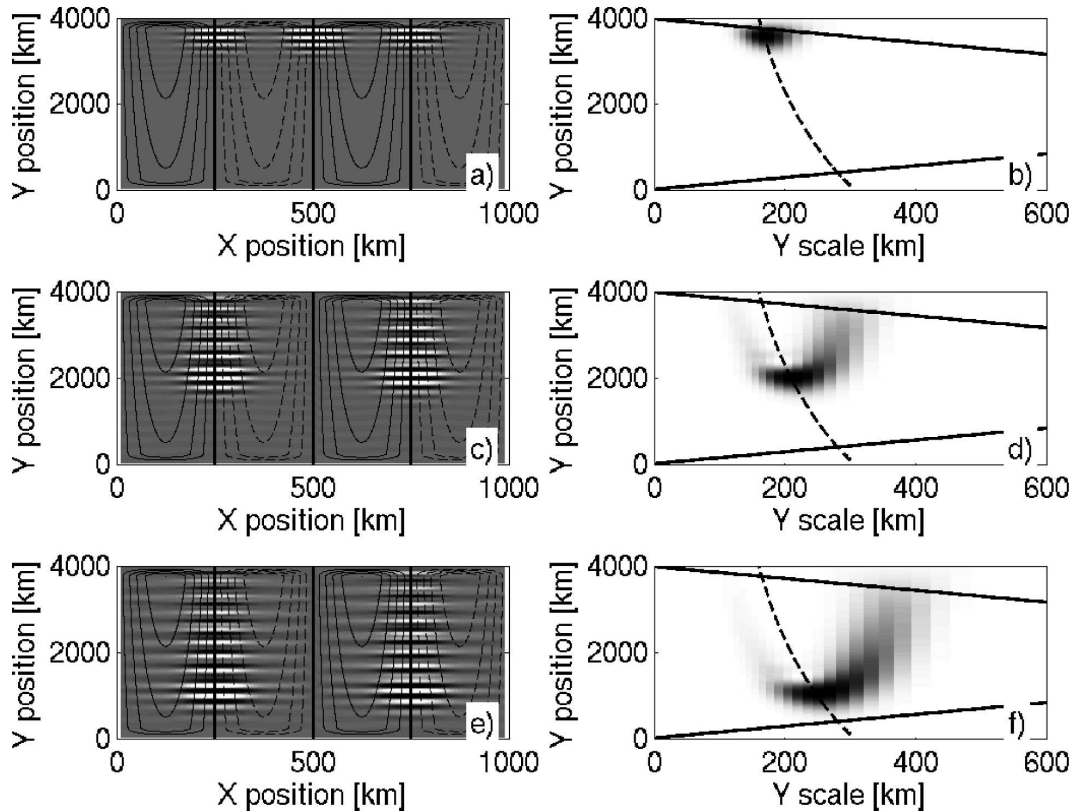
FIG. 1. Eigenmodes (pressure) (a),(b) 1, (c),(d) 20, and (e),(f) 45 of the barotropic perturbations originating from a sin($kx$) basic wave. The eigenmodes are superimposed on the basic wave height field at left. At right are the wavelet transform power spectra, indicating the dominant meridional scales as a function of latitude. The dashed curve shows a scale proportional to the local deformation radius. The upper and lower lines denote the "cones of influence" ("COI") of the wavelet transform; the region of significance lies between the lines. The results outside the lines are adversely affected by the northern and southern boundaries.

scale as a function of latitude from the continuous-wavelet transform (the wavelet software, written by C. Torrence and G. Compo, was available online at http:// paos.colorado.edu/research/wavelets/). The figure indicates that the gravest mode is intensified in the north, while the higher modes have increasingly more structure to the south. We see from the spectra that the modes' meridional scales increase to the south.

Extracting the dominant $y$ scales for all 50 eigenvectors and plotting them against $y$ yields Fig. 2. The dominant scales vary distinctly with the local deformation radius. The scales are, in addition, approximately one-half of the most unstable wavelength predicted from QG theory (LP04).

In Fig. 3 we plot for the 50 eigenvectors the modes' growth rate versus its dominant meridional scale. The growth rates exhibit a linear dependence on the deformation radius, that is, $T \propto L_D/U$, consistent with the scaling given in section 1 (recall the wave has a shear that is constant in $y$). The constant of proportionality,

from a least squares fit, is within a factor of 2 of that predicted by the QG theory.

The higher modes also exhibit growth at the northern latitudes at scales both larger and smaller than the deformation radius (Fig. 1). However, this growth is slower than that occurring near the deformation radius in the lower modes. This suggests that the lower modes will dominate at a given latitude, yielding deformation-scale eddies.

Next, we time step Eqs. (24) and (25), using a fourth-order Runge–Kutta scheme with an adaptive time step. Rather than using the sinusoidal wave of the previous example, we use a wave that is localized initially near the eastern boundary. Such a wave is more useful for illustration and is meant to represent a Rossby wave propagating from the boundary (excited, e.g., by Kelvin waves; Milliff and McWilliams 1994). The wave (Fig. 4) is one wavelength of a sine wave, shifted by a constant so that the height is nonnegative everywhere. The wave height does not vary in $y$ (except near the northern and
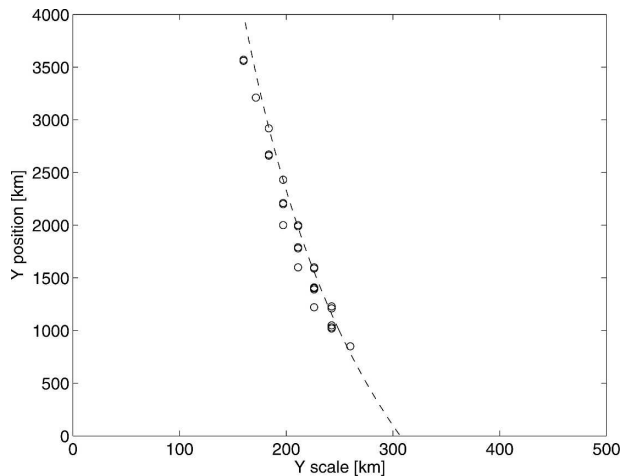
FIG. 2. The dominant meridional scale of the 50 eigenmodes plotted against the latitudes corresponding to the wavelet spectra maxima. The dashed curve indicates one-half of the most unstable wavelength predicted from QG theory [Eq. (3.9a) of LP04], which is proportional to the local deformation radius.
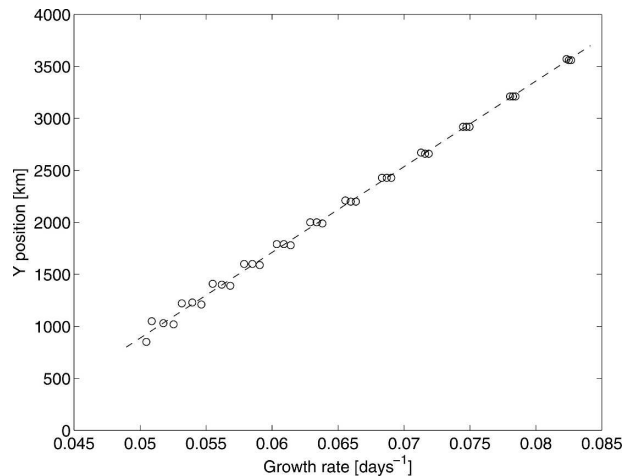


FIG. 3. The modal growth rates plotted against the latitudes of the wavelet spectra maxima. The dashed line comes from a least squares fit and indicates a linear dependence on the deformation radius.

southern boundaries), and we set the wavelength to be 20 times the local deformation radius. Thus the vertical shear, with a value of 10 cm s$^{-1}$, is constant with latitude.

The wave propagates as a long Rossby wave, under Eq. (20). The evolving wave is used for input to the stability equations [(24)–(25)], which are in turn advanced in time. We employ a domain that is 4000 km × 4000 km (spanning roughly 40° latitude), centered at 30°N. The basin depth and stratification were as in the eigenmode calculations. With a shear of 10 cm s$^{-1}$, the $Z$ values range from approximately 0.1 at the southern boundary to about 10 at the northern.

The evolution is depicted in Fig. 5, which shows the basic wave plus the unstable barotropic disturbances at a time not long after initialization. The basic wave propagates faster at low latitudes, causing the familiar latitudinal bending of the crests. The unstable disturbances appear first at high latitudes. The growth at low latitudes is slower.

In the right panel is the meridional spectrum of the disturbances. This shows that the meridional scales are proportional to the local deformation radius. There are larger-scale features in the south, but these are for the most part insignificant (contaminated by boundary contributions).

The temporal growth of the perturbations is indicated in Fig. 6. This shows the rms barotropic pressure averaged in three latitude bands (centered at 860, 1980, and 3100 km). There is clear exponential growth in the upper two latitude bands. The growth continues indefinitely because the unchanging basic wave is effectively

an infinite source of potential energy. Growth has also commenced in the lowest band, but there is little increase before the basic wave strikes the west wall. Rescaling time by the expected growth time $L_D/U$ collapses the curves from the northern two bands on to one another, implying the same scaling in the growth rate. The corresponding (scaled) growth rate is comparable to that predicted by QG theory in the high-$Z$ limit.[2]

Thus, the LQG simulations support the application of QG theory at successive latitudes. The large-scale waves are unstable to deformation-scale perturbations whose growth times scale with the deformation radius. However, the basic wave cannot change in these simulations, meaning we can not see how the perturbations alter the basic wave. For that, we must turn to a full ocean model.

## 4. Primitive equation simulations

The LQG expansion is based on the *assumption* of growth at the deformation radius, and the LQG stability equations closely resemble those in QG. Thus, it may seem unremarkable that the preceding results agree so well with QG theory. What we require is an independent means of examining the wave evolution. For this we employ the ROMS (e.g., Shchepetkin and McWilliams 2005). The model is based on the primitive equations and thus is free of assumptions about the

---

[2] The QG low-$Z$ growth rate for equal-layered depths is $0.1U/L_D$ (LP04). This corresponds to an *e*-folding time of 10 times $L_D/U$. The high-$Z$ growth rate is some 60% faster.
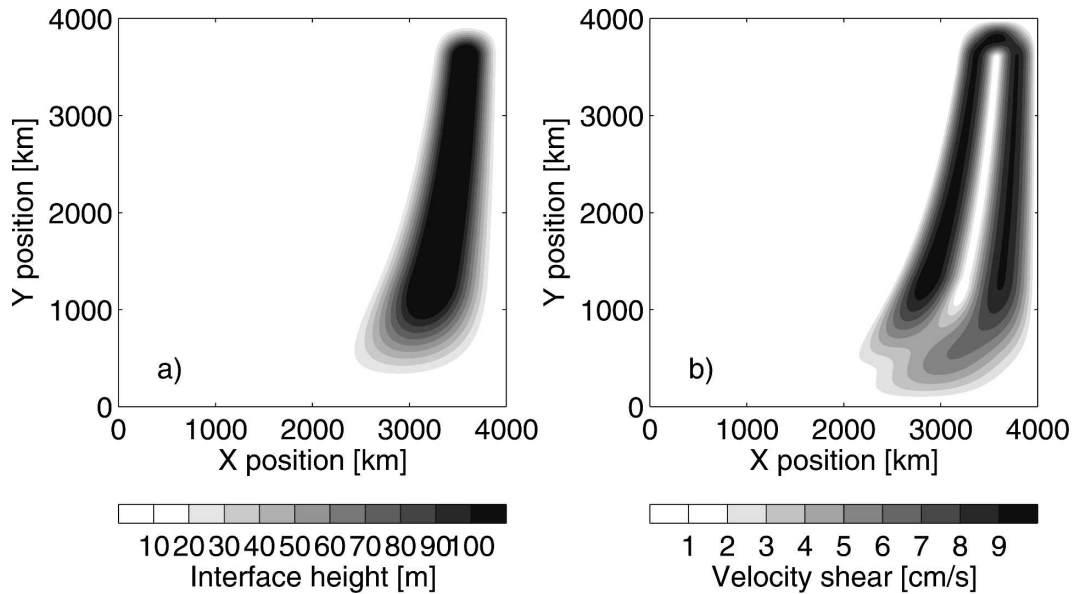
FIG. 4. (left) The eastern basin wave amplitude and (right) its vertical shear. The wavelength is 20 times the local deformation radius at all latitudes.

balances pertaining to perturbations. The model will permit assessing the LQG results and testing definitively whether the waves are unstable.

For the subsequent simulations, we used a spherical grid with a wedge-shaped sector spanning 5°–55°N, 160°–260°E. The model domain had 400 and 200 grid points in the zonal and meridional directions (¼° × ¼°), yielding a maximum horizontal grid spacing of 27 km. The background stratification was linear, with a

buoyancy frequency of 0.0035 rad s$^{-1}$. This is somewhat larger than typical values in the Pacific (Chelton et al. 1998), but yields deformation radii that are resolved by this model grid. In addition, the bottom was flat, with a depth $H = 4000$ m, and we used 10 vertical layers of equal thickness. Explicit mixing and dissipation were switched off, although there is small-scale implicit dissipation associated with the model's third-order advection scheme (e.g., Ferziger and Peric 1999).
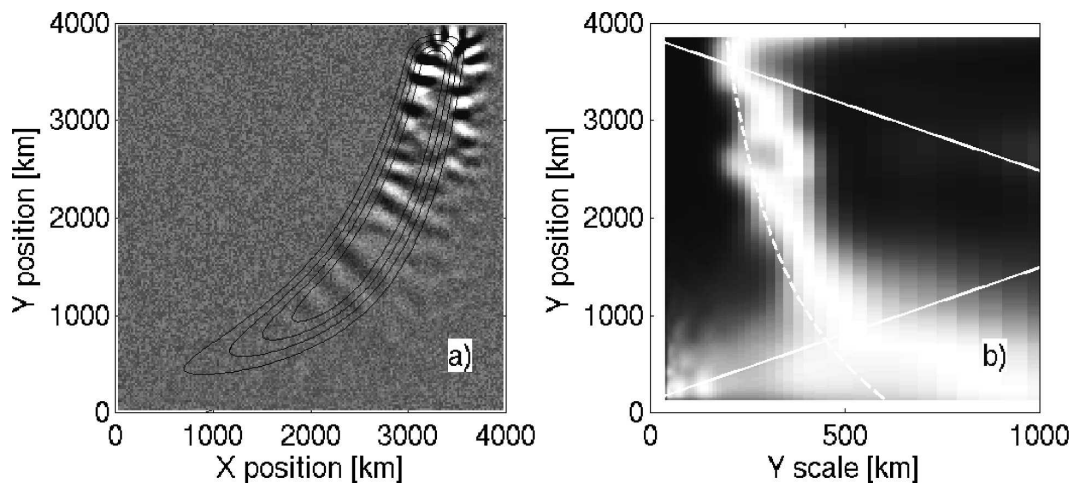


FIG. 5. The LQG solution at day 100 for an isolated wave propagating from the eastern boundary. The wave is shown at left with the barotropic perturbations superimposed. At the right is the wavelet spectrum of the barotropic field, showing the dominant *y* scale as a function of *y* (and normalized by the power at each *y*). The dashed curve indicates one-half of the wavelength of the most unstable wave predicted by QG theory and is proportional to the local deformation radius. The solid lines indicate the COI, defined in Fig. 1.
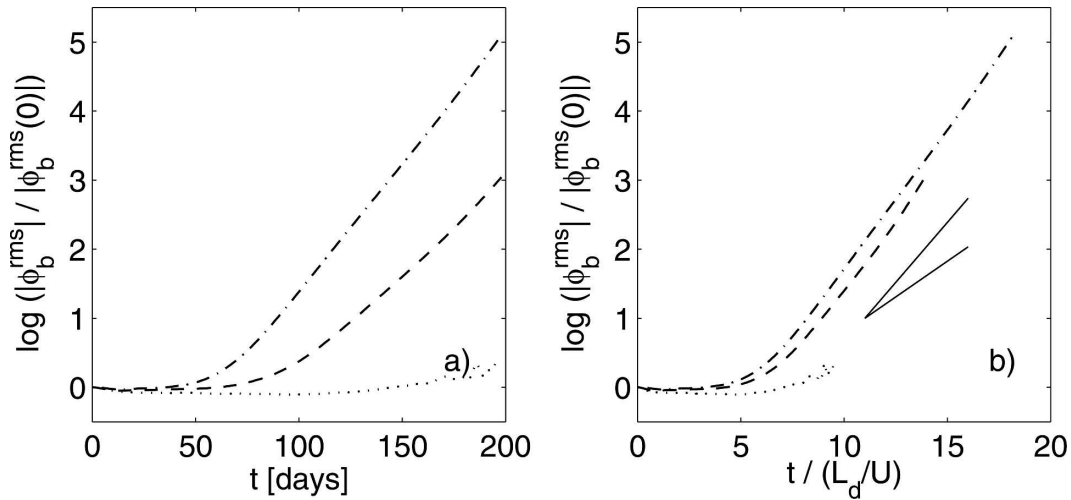
FIG. 6. The rms barotropic pressure for the isolated Rossby wave initiated near the eastern boundary plotted (left) against time and (right) against time rescaled by $L_D/U$. The curves correspond to latitude bands centered at 860 (dotted), 1980 (dashed), and 3100 (dashed–dotted) km. The two solid lines give theoretical growth curves in the low- and high-$Z$ limits from QG theory (LP04).

We initialized the model with a weak-amplitude baroclinic wave, as a perturbation to the linear stratification. This was meant to represent the order–Rossby number baroclinic wave of section (2b). We did not include the higher-order (the order $\epsilon^2$) corrections, but let the model generate those itself; these are occasion-ally visible in the subsequent plots, particularly near the boundaries. We added weaker, random barotropic and baroclinic perturbations at ¹⁄₁₀ the amplitude of the basic wave to catalyze the instability.

We begin with the second case considered in section 3—the isolated wave propagating from the eastern
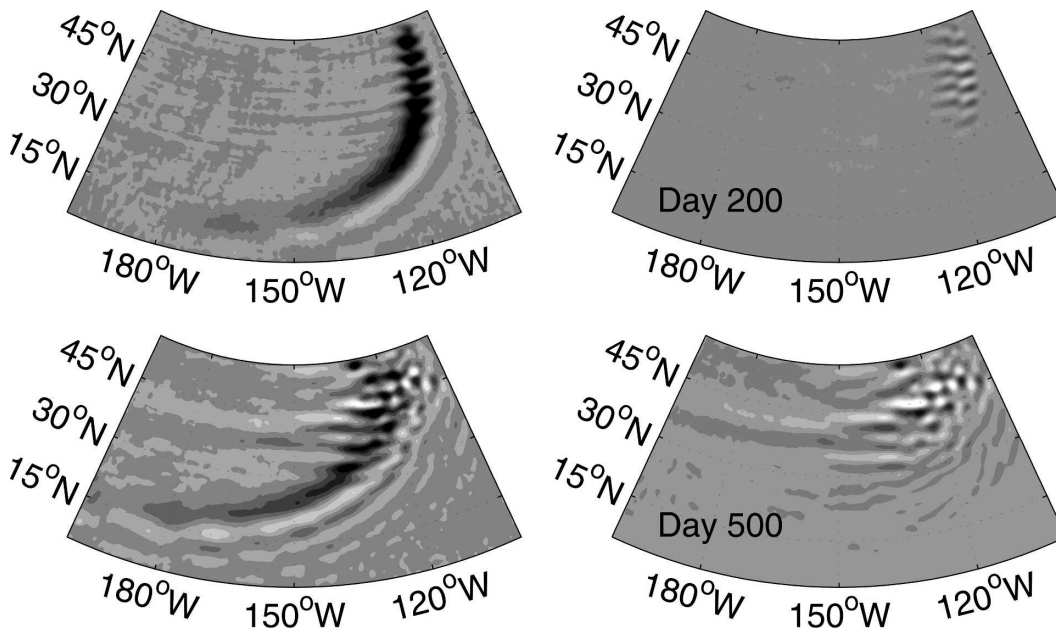


FIG. 7. An initially isolated Rossby wave propagating from the eastern boundary. The wave structure is like that in Fig. 4, that is, a single sine wave with a wavelength of 20 deformation radii. (left) The sea surface elevation and (right) the barotropic height (defined in the text) at days (top) 200 and (bottom) 500 are shown. The shading scale is from −10 to +10 cm.

boundary. The initial condition was similar to that shown in Fig. 4, a single-wavelength sine wave that is 20 deformation radii wide. The wave is shown in Fig. 7 at two different times after initialization. The figure shows the sea surface height and a proxy for the geostrophic barotropic height displacement, defined as

$$\eta_B = \frac{f}{g} \int_{xe-x}^{xe} \bar{v}_B \, dx, \qquad (26)$$

where $\bar{v}_B$ is the depth-averaged meridional velocity and xe is the eastern boundary. The barotropic displacement is useful because it essentially filters out the basic wave, revealing the unstable eddies.

As in the LQG simulation, the instabilities develop first in the north. By day 200, the perturbations north of 30° are as strong as the wave itself and are severely distorting it; by day 500, the wave has broken up in the north and barotropic eddies are radiating to the west. South of 30° there is little unstable growth, and the wave succeeds in reaching the western boundary.

Figure 8 shows the wavelet spectra of the meridional scales derived from the barotropic height field at three latitudes (42°, 30°, and 17°). Again, we use the barotropic height because it is more indicative of the perturbations than the actual surface height. The spectra in the upper two latitude bands suggest unstable growth at a scale proportional to the deformation radius. The dominant wavelength is somewhat larger than the deformation wavelength,[3] and is comparable to (but also somewhat greater than) the scale seen in the LQG simulations. In the northern band, the energy shifts to still-larger scales at around day 500. This reflects an inverse energy cascade as the barotropic eddies merge to produce larger eddies. The cascade ceases, and the scale remains fixed thereafter. In the midlatitude band there is also a shift to larger scales around day 500, but this is much less pronounced than in the north.

In the southern band, there is little indication of unstable growth. Note the energy at scales greater than 800 km is insignificant in the wavelet transform. We observe energy below the deformation radius at late times, but this evidently reflects the southward spreading of the unstable eddies from the north.

Figure 9 shows the growth rates at three latitudes, inferred from the rms barotropic height. The barotropic energy is clearly increasing in all three bands. It is difficult to say whether the growth is exponential in time,

---

[3] Note that the denominator of the dimensional Rossby dispersion relation is $k^2 + l^2 + L_D^{-2}$, where $k$ and $l$ are the zonal and meridional wavenumbers, respectively, and so the wavelength corresponding to $L_D^{-1}$ is $2\pi L_D \approx 6.3 L_D$. The dominant scale seen in the figure, roughly $8L_D$, is thus 1.3 times this value.
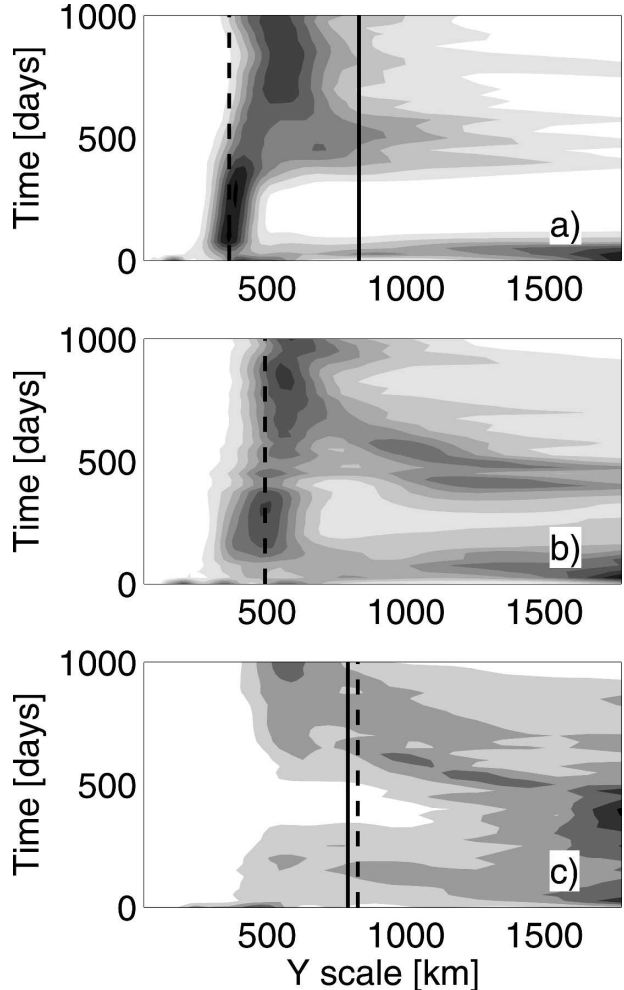


FIG. 8. Wavelet spectra of meridional scale as a function of time, generated from the barotropic height at (top) 42°, (middle) 30°, and (bottom) 17° latitude. The dashed line indicates 1.3 times the deformation wavelength. The solid lines for the northern and southern latitudes are the COI of the transform; the spectra are insignificant to the right of the COI.

but the growth in the northern and midlatitude bands is similar when plotting against time rescaled by $L_D/U$ (right panel). The late time increase in the southern latitude band probably reflects the southward spreading of eddies generated in the north.

After a time of about $20–30L_D/U$, the barotropic energy levels off in the northern and middle bands. The final energy level is greatest in the north, implying a more energetic barotropic eddy field here. This stems from having a constant wave shear, because there is more potential energy at high latitudes to be tapped by the instability. Note that the barotropic energy in the northern band saturates at about 400 days, which is roughly the same time that the barotropic energy shifts to larger scales (Fig. 8). Thus, saturation is coincident
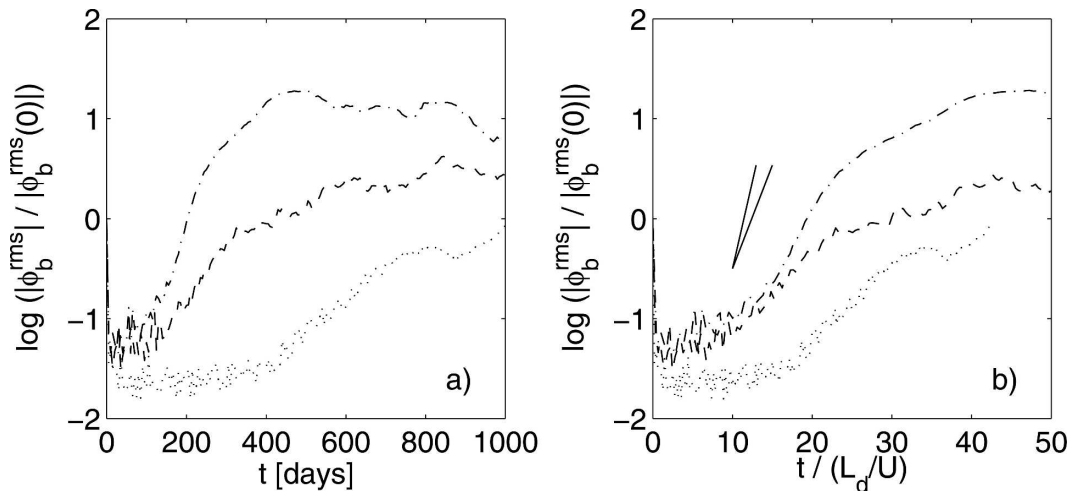
FIG. 9. The rms barotropic height, averaged in three latitude bands centered at 42° (dashed–dotted), 30° (dashed), and 17° (dotted), as functions of time. The rms heights are normalized by their initial values. The values are plotted against time on the left and against time rescaled by $L_D/U$ on the right. The two solid lines indicate the low- and high-$Z$ growth rates from QG theory (LP04).

with the beginning of the energy cascade. The same effect was observed in the QG simulations of LP04.

Then we examined a basin-spanning sinusoidal wave, as in the eigenvalue calculations in section 3. The evolution of the height fields, shown in Fig. 10, is qualitatively the same as that with the isolated wave. The wave breaks up in the north after several hundred days, and thereafter the northern latitudes are filled with barotropic eddies.

The evolution in the meridional scales as seen in the

wavelet spectra is shown in Fig. 11. As before, energy appears initially at roughly 8 times the deformation radius in the northern and midlatitude bands while there is much less indication of unstable growth in the southern band. Interestingly, the energy in the northern band begins to shift to larger scales at around day 300, which is earlier than in the eastern wave case, and then proceeds to still-larger scales.

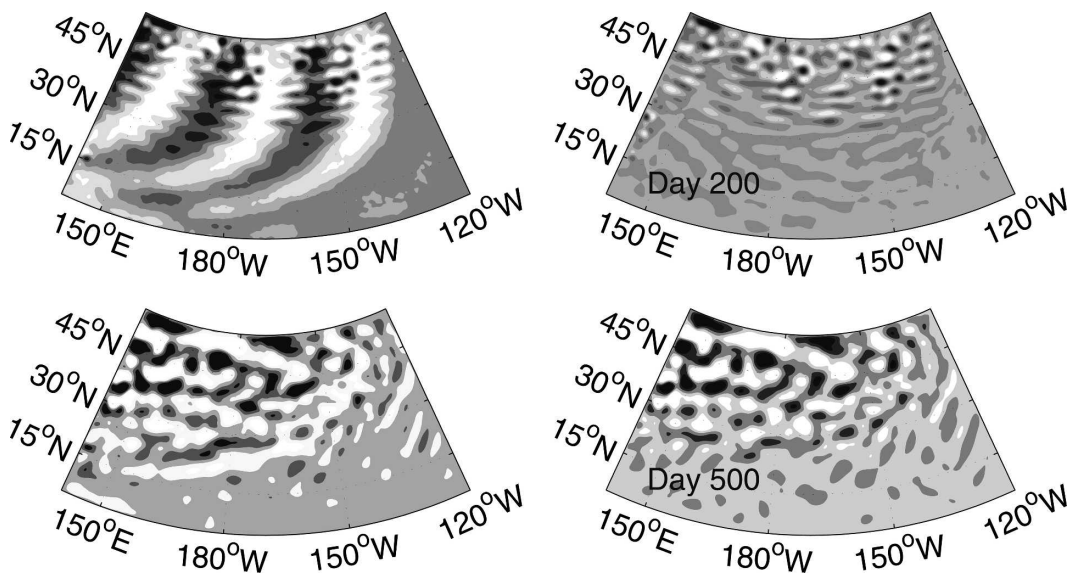Comparing the two cases, we infer that the inverse cascade is more energetic in the basin-spanning wave



FIG. 10. (left) The sea surface elevation and (right) the barotropic height (defined in the text) at days (top) 200 and (bottom) 500 for the initial sine wave are shown. The shading scale is from −20 to 20 cm.
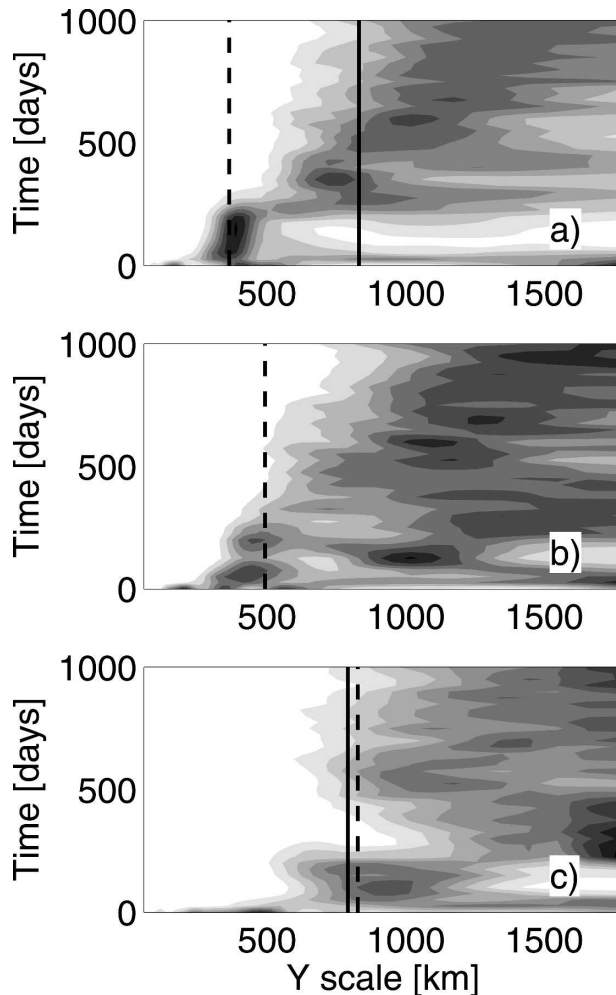
FIG. 11. The wavelet spectra from the sine wave case. As before, the spectra were obtained from the barotropic height, averaged in three latitude bands at (top) 42°, (middle) 30°, and (bottom) 17° latitude. The dashed line indicates the same scale as in Fig. 8, or 8 times the deformation radius. The solid lines in the top and bottom panels are the COI.

case. This is most likely because that case has a more homogeneous barotropic eddy field. Unstable perturbations grow in the east *and* the west, and these eddies merge with one another. With the isolated wave the unstable eddies emerge only in the east, so the cascade proceeds essentially only to the scale of the initial wave. The inhomogeneity of the eddy field thus causes the inverse cascade to cease, an effect noted by Rhines (1977). But with barotropic eddies across the basin, the cascade can proceed further upscale.

The growth curves from the three latitude bands are shown in Fig. 12. The curves indicate exponential growth, with rates that scale with $L_D/U$ (and are comparable to that predicted by QG theory). The growth saturates after roughly 15–20 times $L_D/U$, again at

about the same time as the barotropic energy shifts toward larger scales. The saturation energies are higher in the north, although the differences between latitudes are less than with the eastern wave.

The ROMS simulations thus support the predictions of the LQG theory. The baroclinic Rossby wave is unstable to perturbations that grow at a scale proportional to the local deformation radius $L_D$, with a growth rate proportional to $U/L_D$. Distinct from the LQG simulations is that the perturbations grow to finite amplitude and merge, allowing for an inverse energy cascade. The cascade is more energetic at high latitudes, resulting in part from our choice of waves with constant shear.

## 5. Phase speeds

The seminal satellite observations of Chelton and Schlax (1996) suggested that the westward-propagating sea surface height anomalies outside the Tropics move faster than the baroclinic long-wave speed. Subsequent theories attributed these increased phase speeds to a number of factors, including the interaction between the baroclinic mean circulation (Killworth et al. 1997) and topography (Tailleux and McWilliams 2001).

As noted, LP04 suggested that wave instability might be responsible for this, if the height anomalies reflect *barotropic* rather than baroclinic Rossby waves. The most unstable barotropic wave from the QG theory has a phase speed that is roughly 2 times the long-wave speed.

Here we consider the phase speeds in the ROMS simulations, as deduced from Hovmoeller diagrams of the sea surface height. We use the sea surface height rather than the barotropic displacement because satellites measure the former. Figure 13 shows the isolated eastern wave case at the center latitudes from the three bands examined before. The two lines in the figure indicate the baroclinic long-wave speed (the dashed line) and the barotropic wave speed (2.4 times the long-wave speed; the solid line) predicted by LP04. Figure 14 shows the same diagrams from the sinusoidal wave case.

In both cases, the crests at the southernmost latitude band propagate at or near the long-wave speed for the duration of the experiment.[4] At the mid- and high latitudes, the speeds increase during the experiment. At the northern-most latitude, the increase is evident after about 400 days in the eastern wave case and after 200

_____

[4] The additional crests in the eastern wave case are from shorter waves, originating from the eastern boundary and propagating slower than the long-wave speed.
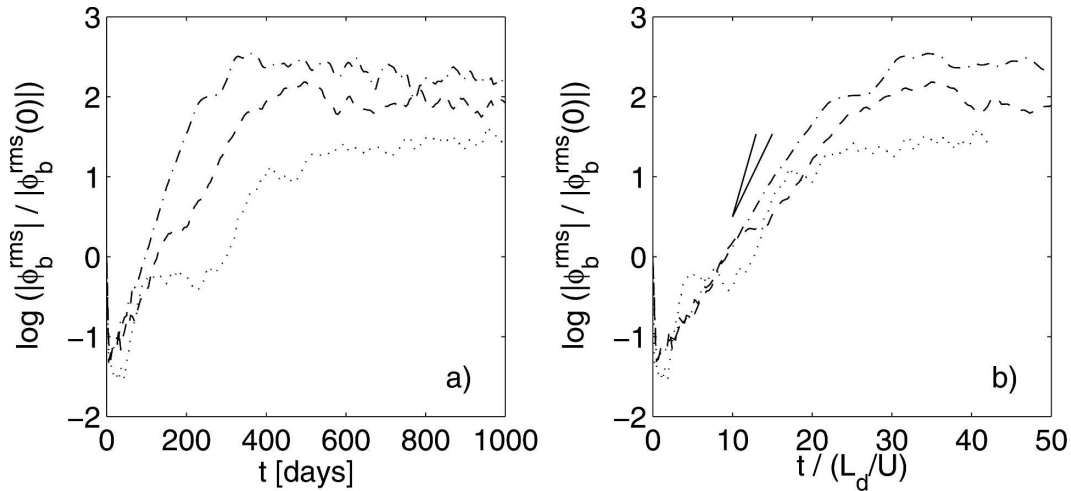
FIG. 12. As in Fig. 9, the rms barotropic height in the three latitude bands for the sine wave case, plotted against time and time rescaled by $L_D/U$.

days in the sine wave case. The faster speeds in the eastern wave case are comparable to the QG prediction. However, they are even *faster* in the sine wave case.

The transitions to faster phase speeds occur at the same time as the growth in barotropic energy saturates (Figs. 9 and 12). As mentioned, this is also the time when the barotropic energy begins to shift toward larger meridional scales (Figs. 8 and 11). Thus, the phase speed increase is visible *after* the baroclinic wave has broken up, but not during the growth phase. The latter follows from the fact that the perturbations grow in the high-shear regions and propagate *with* the basic wave. Thus their phase speeds during the growth period are similar to the long-wave speed. Something like this also occurs in the QG case in the high-$Z$ limit (LP04). The increased phase speed is not evident before the basic wave vanishes because the perturbations are essentially riding piggyback on the basic wave.

The faster phase speeds in the sine wave case occur because of the inverse cascade. As noted, the cascade ceases in the eastern wave case because the barotropic eddy field is localized. The eddies are roughly as large as when they are formed, and propagate at the predicted speed. But, the sine wave case yields a barotropic eddy field that spans the basin, facilitating mergers and then larger, and thus faster, barotropic waves.

We summarize the phase speed dependence on latitude in Fig. 15, which compares the speeds deduced from the Hovmoeller diagrams with the long-wave speed. With the eastern wave, the speeds are comparable to the long-wave speed south of 30° and are 2–3 times as high to the north. This is qualitatively consistent with the picture shown in Chelton and Schlax (1996, their Fig. 5). In the sine wave case, the phase speeds north of 20° are even faster, up to 10 times faster than the long-wave speed. Because such speeds are greatly in excess of those of Chelton and Schlax, we suspect that such a vigorous cascade is probably not occurring. Thus the eastern wave case is perhaps the more realistic one.

## 6. Summary and conclusions

We have generalized the quasigeostrophic stability theory of LP04 to a realistically large ocean basin. To do this, we expanded the two-layer shallow-water equations by assuming a small-amplitude basin-scale wave and derived a pair of coupled stability equations. We refer to these as the "LQG" equations because the disturbances, anticipated to be of deformation scale, are locally quasigeostrophic. The LQG equations are similar to the barotropic/baroclinic QG vorticity equations, except that they retain a realistic variation of the internal deformation radius.

We used these equations to calculate eigenmodes, assuming the wave was stationary to leading order. The eigenmodes suggested that the most rapid growth at any latitude occurs near the deformation radius on a time scale proportional to $L_D/U$. Thus, instability proceeds most rapidly at high latitudes. Time stepping the equations yielded similar results and implied that only at southern latitudes could the wave cross the basin before the instabilities had grown appreciably.

The results are thus in line with what would be expected by applying QG theory at successive latitudes. However, the LQG equations are very similar to their QG counterparts. Thus we used a primitive equation model (ROMS) to obtain an independent confirmation.
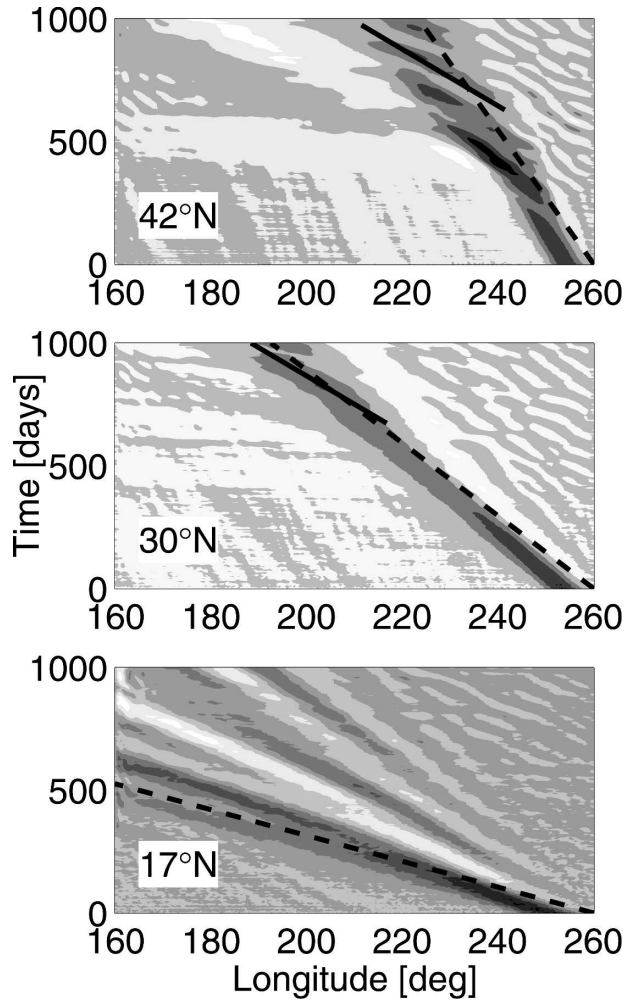
FIG. 13. Hovmoeller diagrams from the ROMS simulation of the isolated eastern wave. The diagrams were constructed from the sea surface height at the center latitudes from the three latitude bands examined earlier. The dashed line indicates the long-wave speed, and the solid line is 2.4 times that speed.
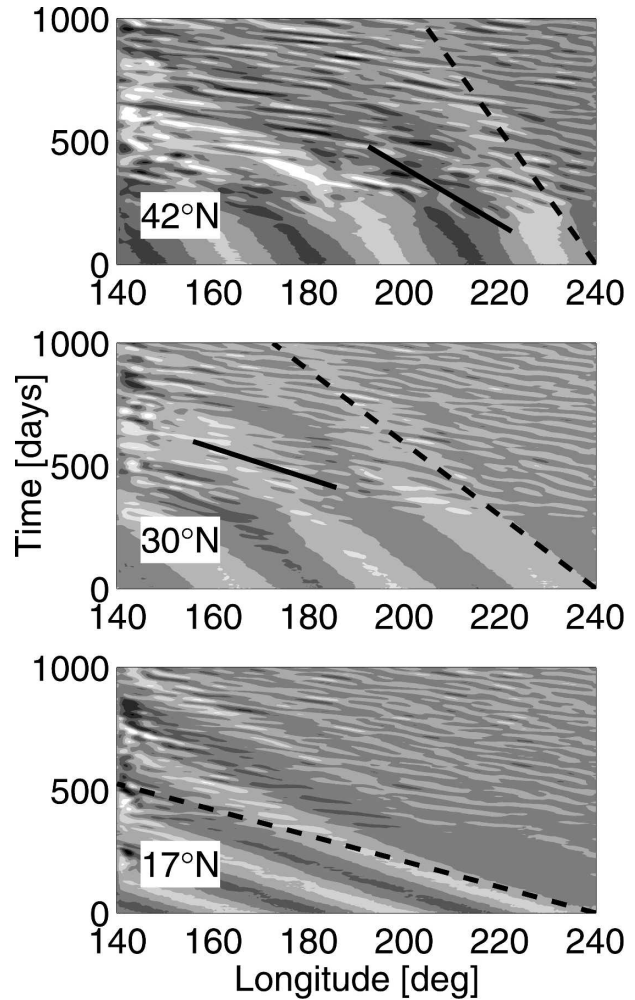
FIG. 14. As in Fig. 13, Hovmoeller diagrams from the ROMS simulation of the sinusoidal wave. The dashed line indicates the long-wave speed, and the solid line is 2.4 times that speed.

The ROMS results were in accord with the LQG results, showing unstable growth near the local deformation radius with a time scale proportional to $L_D/U$.

Last, we examined the westward phase speeds, which are apparent in the surface height field. As suggested by LP04, there is an increase in the speed following instability, because the barotropic waves (which have a surface expression) propagate faster than the baroclinic long-wave speed. The increases found with an isolated wave emanating from the eastern wall were in good agreement with the satellite observations of Chelton and Schlax (1996).

Though we did not discuss it here, we also examined the instability of baroclinic basin modes. Indeed, the present work (and that of LP04) was motivated by the question of whether these modes are unstable. Basin modes have very large scales and low frequencies and are thus of potential interest for climate variability (LaCasce 2000; Cessi and Primeau 2001; Primeau 2002; LaCasce and Pedlosky 2002; Ben Jelloul and Huck 2003). We performed simulations of several different modes using both the LQG and ROMS models, and in all cases the modes were unstable. The instabilities grow fastest in the northwest, where the shear is greatest. However, the conclusion is the same—the modes, like isolated Rossby waves, break up at the northern latitudes.

Our focus has been on waves with fixed vertical shear, but oceanic waves emanating from eastern boundaries will have different amplitudes, depending on the forcing. This will impact the degree of penetration into the basin, by altering the unstable growth
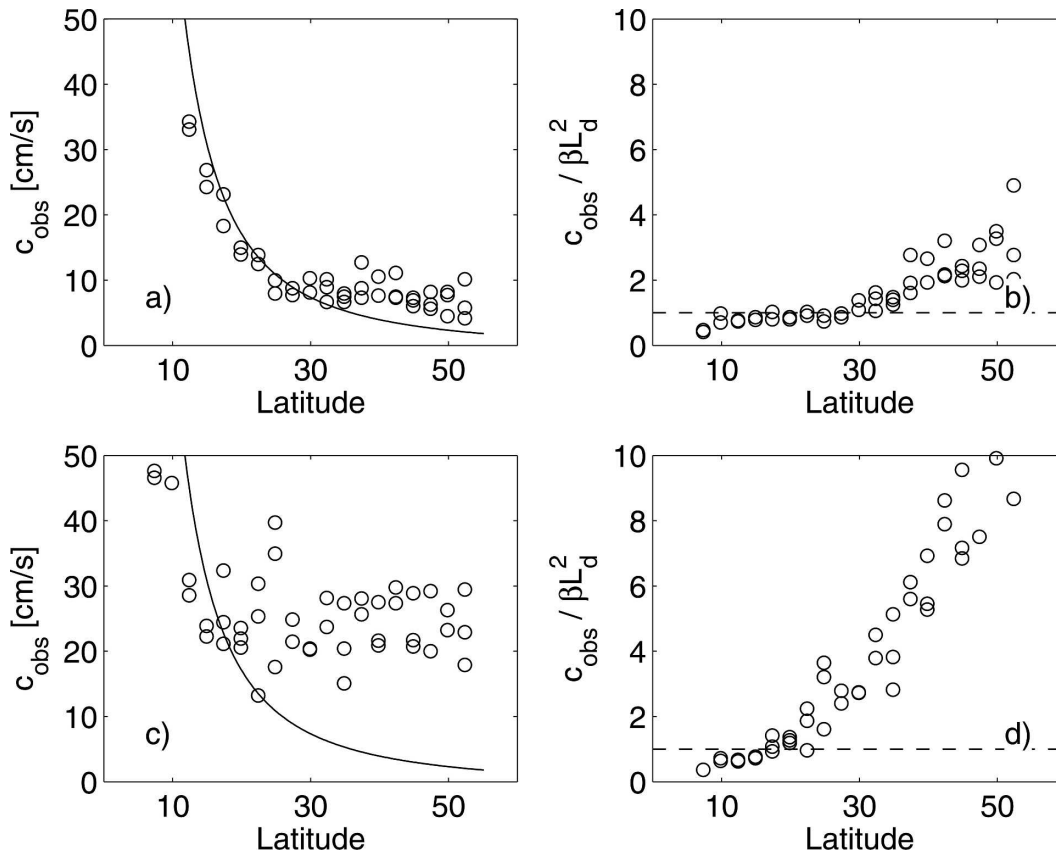
FIG. 15. (left) The westward phase speeds deduced from Hovmoeller diagrams of the sea surface height in the ROMS experiments with (top) the isolated eastern wave and (bottom) the basin-spanning wave. We extracted the speeds at the higher latitudes during the period just after the phase speed acceleration; at low latitudes, we extracted the speed from the leading wave crest. (right) The ratios of observed speed to the long-wave speed. A more vigorous inverse cascade is responsible for the larger phase speeds in the bottom panels.

times. We have also neglected mean flow effects. However, if the primary dynamic is that of waves radiating from the eastern boundary, then such waves may not have a chance to encounter significant mean flow, intensified in the west, before succumbing to instability. This remains to be seen of course, with more realistic models. We have also focused on weak-amplitude waves, because finite-amplitude waves would steepen in time (section 2b). We note though that such waves would have *greater* vertical shear and thus might be even more prone to instability. The analogous stability equations for an order of one baroclinic wave are similar to those considered here, but with additional terms resulting from barotropic interactions; they could be studied in the future.

As suggested by LP04, wave instability may explain the observed phase speeds derived from sea surface height data in the Pacific. An alternate way of looking at this is that the observed waves have frequencies that are too high. Zang and Wunsch (1999) and Fu and

Chelton (2000) superimposed sea surface height–derived wavenumber spectra over the baroclinic wave dispersion relation and found that this was true. Moreover, rather than following the shape of the baroclinic dispersion curve (which has a maximum at the deformation radius), the data clustered around a line. This implies a constant phase speed (at a given latitude). In contrast, the baroclinic dispersion curve is only linear at the largest scales.

We would expect a constant phase speed at a given latitude of 2–3 times the long-wave speed. However, our results cannot necessarily explain why there is such a range of wave scales all propagating at that speed. To understand this further, it would be useful to know the relative contributions to the wavenumber spectra at the different wavelengths. Is the energy evenly distributed or intensified over a small range of scales near the deformation radius?

There is also the fate of the barotropic eddies. Comparing our results with the satellite observations of

Chelton and Schlax (1996), it appears there is little in the way of an inverse cascade after instability. Such a cascade might be arrested by the $\beta$ effect (Rhines 1977), but altimeter data suggest that the dominant eddy scales are poorly correlated with the arrest scale (Stammer 1997). The cascade, on the other hand, could be halted either by the inhomogeneity of the eddy field or by another effect like topography. However, either way, the product of the instability would appear to be deformation-scale barotropic Rossby waves.

Last, Rossby wave instability could have profound implications for the adjustment of wind-driven oceanic flows. Our general conception of the response to changing winds, following Anderson and Gill (1975), is one mediated by Rossby waves propagating from the eastern boundary. The passage of the baroclinic waves alters the baroclinic structure of the general circulation. Instability of the baroclinic waves will presumably alter this process significantly.

## REFERENCES

Anderson, D. L. T., and A. E. Gill, 1975: Spin-up of a stratified ocean with application to upwelling. *Deep-Sea Res., 22,* 583–596.

Ben Jelloul, M., and T. Huck, 2003: Basin-mode interactions and selection by the mean flow in a reduced-gravity quasigeostrophic model. *J. Phys. Oceanogr., 33,* 2320–2332.

Cessi, P., and F. Primeau, 2001: Dissipative selection of low-frequency modes in a reduced-gravity basin. *J. Phys. Oceanogr., 31,* 127–137.

Charney, J. G., and G. R. Flierl, 1981: Oceanic analogues of large-scale atmospheric motions. *The Evolution of Physical Oceanography,* C. Wunsch and B. Warren, Eds., MIT Press, 504–548.

Chelton, D. B., and M. G. Schlax, 1996: Global observations of oceanic Rossby waves. *Science, 272,* 234–238.

——, R. A. de Szoeke, M. G. Schlax, K. El Naggar, and N. Siwertz, 1998: Geographical variability of the first-baroclinic Rossby radius of deformation. *J. Phys. Oceanogr., 28,* 433–460.

Ferziger, J. H., and M. Peric, 1999: *Computational Methods for Fluid Dynamics.* Springer-Verlag, 400 pp.

Fu, L.-L., and D. B. Chelton, 2000: The large-scale ocean circulation. *Satellite Altimetry and Earth Sciences: A Handbook of Techniques and Applications,* L.-L. Fu and A. Cazenave, Eds., Academic Press, 133–170.

Jones, S., 1979: Rossby wave interactions and instabilities in a rotating two-layer fluid on a beta-plane. Part I. Resonant interactions. *Geophys. Astrophys. Fluid Dyn., 11,* 289–322.

Killworth, P. D., D. B. Chelton, and R. A. de Szoeke, 1997: The speed of observed and theoretical long extratropical planetary waves. *J. Phys. Oceanogr., 27,* 1946–1966.

LaCasce, J. H., 2000: Baroclinic Rossby waves in a square basin. *J. Phys. Oceanogr., 30,* 3161–3178.

——, and J. Pedlosky, 2002: Baroclinic Rossby waves in irregular basins. *J. Phys. Oceanogr., 32,* 2828–2847.

——, and ——, 2004: The instability of Rossby basin modes and the oceanic eddy field. *J. Phys. Oceanogr., 34,* 2027–2041.

Milliff, R. F., and J. C. McWilliams, 1994: The evolution of boundary pressure in ocean basins. *J. Phys. Oceanogr., 24,* 1317–1338.

Pedlosky, J., 1984: The equations for geostrophic motion in the ocean. *J. Phys. Oceanogr., 14,* 448–455.

——, 1987: *Geophysical Fluid Dynamics.* Springer, 728 pp.

Primeau, F., 2002: Long Rossby wave basin-crossing time and the resonance of low-frequency basin modes. *J. Phys. Oceanogr., 32,* 2652–2665.

Rhines, P., 1977: The dynamics of unsteady currents. *The Sea,* E. D. Goldberg, Ed., Marine Modeling, Vol. 6, Wiley Interscience, 189–318.

Shchepetkin, A. F., and J. C. McWilliams, 2005: The Regional Oceanic Modeling System (ROMS): A split-explicit, free-surface, topography-following-coordinate oceanic model. *Ocean Modell., 9,* 347–404.

Stammer, D., 1997: Global characteristics of ocean variability estimated from regional Topex/Poseidon altimeter measurements. *J. Phys. Oceanogr., 27,* 1743–1769.

Tailleux, R., and J. C. McWilliams, 2001: The effect of bottom pressure decoupling on the speed of extratropical, baroclinic Rossby waves. *J. Phys. Oceanogr., 31,* 1461–1476.

Theiss, J., 2004: Equatorward energy cascade, critical latitude, and the predominance of cyclonic vortices in geostrophic turbulence. *J. Phys. Oceanogr., 34,* 1663–1678.

Vanneste, J., 1995: Explosive resonant interaction of baroclinic Rossby waves and stability of multilayer quasi-geostrophic flow. *J. Fluid Mech., 291,* 83–107.

Zang, X., and C. Wunsch, 1999: The observed dispersion relationship for North Pacific Rossby wave motions. *J. Phys. Oceanogr., 29,* 2183–2190.